The Astrophysical Journal Letters, 896:L9 (8pp), 2020 June 10 https://doi.org/10.3847/2041-8213/ab961e

On the Lorentz Force and Torque of Solar Photospheric Emerging Magnetic Fields

Aiying Duan[1], Chaowei Jiang[2], Shin Toriumi[3], and Petros Syntelis[4]
[1] Planetary Environmental and Astrobiological Research Laboratory (PEARL), School of Atmospheric Sciences, Sun Yat-sen University, Zhuhai 519000, People's Republic of China; duanaiy@mail.sysu.edu.cn
[2] Institute of Space Science and Applied Technology, Harbin Institute of Technology, Shenzhen 518055, People's Republic of China; chaowei@hit.edu.cn
[3] Institute of Space and Astronautical Science (ISAS)/Japan Aerospace Exploration Agency (JAXA), 3-1-1 Yoshinodai, Chuo-ku, Sagamihara, Kanagawa 252-5210, Japan
[4] School of Mathematics and Statistics, St. Andrews University, St. Andrews, KY16 9SS, UK
Received 2020 April 10; revised 2020 May 18; accepted 2020 May 19; published 2020 June 9

Abstract

Magnetic flux generated and intensified by the solar dynamo emerges into the solar atmosphere, forming active regions (ARs) including sunspots. Existing theories of flux emergence suggest that the magnetic flux can rise buoyantly through the convection zone but is trapped at the photosphere, while its further rising into the atmosphere resorts to the Parker buoyancy instability. To trigger such an instability, the Lorentz force in the photosphere needs to be as large as the gas pressure gradient to hold up an extra amount of mass against gravity. This naturally results in a strongly non-force-free photosphere, which is indeed shown in typical idealized numerical simulations of flux tube buoyancy from below the photosphere into the corona. Here we conduct a statistical study of the extents of normalized Lorentz forces and torques in the emerging photospheric magnetic field with a substantially large sample of Solar Dynamics Observatory/Helioseismic and Magnetic Imager vector magnetograms. We found that the photospheric field has a rather small Lorentz force and torque on average, and thus is very close to a force-free state, which is not consistent with theories as well as idealized simulations of flux emergence. Furthermore, the small extents of forces and torques seem not to be influenced by the emerging AR's size, the emergence rate, or the nonpotentiality of the field. This result puts an important constraint on future development of theories and simulations of flux emergence.

Unified Astronomy Thesaurus concepts: Solar magnetic fields (1503); Solar photosphere (1518)

1. Introduction

Sunspots and solar active regions (ARs) are believed to be generated by magnetic flux emerging through the solar surface, i.e., the photosphere (Parker 1955). In the first place, magnetic field is generated by the solar dynamo action in the deep convection zone. Then the magnetic fluxes are further intensified and adopt the form of flux bundles because of stretching and twisting of their magnetic field lines by turbulent fluid motions in the convection zone. Eventually, the flux bundles are pushed up by magnetic buoyancy and rise into the photosphere to form ARs.

Since we are not able to observe directly the process in the subphotospheric layers, most of the knowledge on flux emergence comes from theoretical models and numerical MHD simulations (Archontis 2008; Cheung & Isobe 2014; Archontis & Syntelis 2019). Many simulations show that a flux tube, generally twisted, experiences a typical two-stage emergence process (e.g., Toriumi & Yokoyama 2010) during its passage from the convection zone into the atmosphere, i.e., the solar corona. In the first stage, the magnetic buoyancy force pushes upward the flux tube through the convection zone (Parker 1955), but it is trapped at the shallow layers near the solar surface because of the strongly subadiabatic stratification (i.e., much smaller temperature gradient than an adiabatic stratification) of the photosphere (e.g., Syntelis et al. 2019). Then in the second stage, with more and more magnetic flux pileup just below the surface, the magnetic pressure gradient increases continuously and eventually the Parker instability (Shibata et al. 1989; Archontis et al. 2004), a kind of magnetic Rayleigh–Taylor instability, is triggered to let part of the flux break through the dense photosphere, which is typically observed as a continuous magnetic flux increasing on the photosphere during the emerging of an AR.

To trigger the Parker instability at the subadiabatic photosphere, the Lorentz force must be built up such that it can support against gravity an extra amount of mass comparable to what is supported by the photospheric gas pressure gradient (Newcomb 1961; Acheson 1979; Archontis et al. 2004). Meanwhile the plasma β (ratio of plasma pressure to magnetic pressure) is on the order of unity in the photosphere (Gary 2001; Cho et al. 2017). Thus, in the photosphere, the magnitude of Lorentz force should be comparable to that of the magnetic pressure gradient, and so the emerging field in the photosphere is far from a force-free state in which the Lorentz force vanishes as a result of the balancing between magnetic pressure force and magnetic tension (Wiegelmann & Sakurai 2012). Furthermore, once the buoyancy instability is triggered, the emergence runs into a dynamic phase in which there is a strong interaction of the magnetic field with the plasma, and the field cannot be force-free. However, when the field emerges into the atmosphere by a few scale heights above the photosphere, it relaxes quickly to a closely force-free state because of the fast decreasing of the plasma density and pressure with height (Fan 2009). Thus the distribution of the Lorentz force above the solar surface should be restricted mainly within a small height. To quantify the global extent of this force, one can make use of the Gauss's law by expressing the net volumetric Lorentz force above the photosphere in a surface integral of Maxwell stress tensor of the photospheric magnetic field (Molodenskii 1969; Aly 1984; Low 1985; Fisher et al. 2012, see the formula in Section 2), which are observable and thus the results can be used to compare with and constrain theories and simulations. There have been several works done to estimate the global

Lorentz force of ARs using the observed vector magnetograms from different instruments (Metcalf et al. 1995; Moon et al. 2002; Tiwari 2012; Liu et al. 2013; Liu & Hao 2015), and some of them conclude that the photospheric field is actually not far from force-free (e.g., Moon et al. 2002; Tiwari 2012). However all the previous studies are carried out using the snapshots of developed ARs without considering the case of flux-emerging ARs.

In this Letter, we perform a systematic survey of the global force focusing on ARs in their full emergence phase and using the vector magnetograms from Solar Dynamics Observatory/Helioseismic and Magnetic Imager (SDO/HMI; Hoeksema et al. 2014), which are both done for the first time. Furthermore, in addition to checking the global force, we also estimate the global Lorentz torque, which has not been considered in previous investigations. Our results show that the emerging photospheric fields are actually very close to the force-free state, which is not consistent with the results from typical idealized simulations of twisted flux tube emerging from below the photosphere. This result puts an important constraint on the future development of theories and simulations of flux emergence.

2. Method and Data

Since the Lorentz force can be expressed as the divergence of a tensor, the Maxwell stress, the integration of force in a volume can be expressed as the surface integral of the tensor. Furthermore, by assuming that the emerging magnetic field above the photosphere (i.e., $z > 0$) is well isolated and its strength falls off fast enough going upward to infinity, the net Lorentz force $\boldsymbol{F} = \int \boldsymbol{J} \times \boldsymbol{B} dV$ in the volume of $z > 0$ can be expressed as integration of the Maxwell stress tensor on the photosphere $z = 0$, which is given by (Aly 1984; Low 1985; Fisher et al. 2012)

$$F_x = -\frac{1}{4\pi}\int B_x B_z dxdy,$$
$$F_y = -\frac{1}{4\pi}\int B_y B_z dxdy,$$
$$F_z = -\frac{1}{8\pi}\int (B_z^2 - B_x^2 - B_y^2) dxdy. \quad (1)$$

We note that the same formula can also apply to the interior volume below the surface (by removing the minus sign before the integrations) if the magnetic field below the surface is also well isolated, which, however, is not generally fulfilled unless the surface integration is taken for the full sphere.

To compare the forces in different magnetic fields with different flux contents, it is better to use a normalized measurement. We follow Low (1985) and Metcalf et al. (1995) by employing the integrated magnetic pressure force F_p given by

$$F_p = \left| \int \nabla \left(\frac{B^2}{8\pi} \right) dV \right| = \frac{1}{8\pi}\int (B_x^2 + B_y^2 + B_z^2) dxdy, \quad (2)$$

and the normalized forces are ratios defined as $f_x = |F_x|/F_p$, $f_y = |F_y|/F_p$, and $f_z = |F_z|/F_p$, respectively. For a field being close to force-free, it must have all the ratios much less than unity, i.e., $f_x \ll 1$, $f_y \ll 1$, and $f_z \ll 1$ (Low 1985). Metcalf et al. (1995) suggested that the magnetic field can be considered as force-free completely if the normalized forces are all less than or equal to 0.1, and this criterion is widely accepted by the later studies (Moon et al. 2002; Tiwari 2012; Liu et al. 2013; Liu & Hao 2015; Jiang & Zhang 2019). On the other hand, for a strongly non-force-free field, the ratios can be close to unity, meaning that the magnetic pressure force and the tension force are so unbalanced that the net Lorentz force is comparable to one of its components, the total magnetic pressure force. The HMI team (Sun 2014) released a data set, `cgem.Lorentz`, which also contains the integrated Lorentz forces of the HMI vector magnetograms. A minor difference exists between the horizontal normalized forces we defined here and the ones in `cgem.Lorenzt`, i.e., ϵ_x and ϵ_y, and ϵ_z in Equation (4) in Sun (2014), which are related by $f_x = 2|\epsilon_x|$, $f_y = 2|\epsilon_y|$, and $f_z = |\epsilon_z|$. We use the `cgem.Lorentz` data to verify our calculations.

It should be noted that these ratios being less than 0.1 is only a necessary condition for the fields to be force-free; even if the global integration of force is zero, the forces locally in different parts are not necessarily zero (for example, near the edge of a sunspot, where the local Lorentz force is balanced by gas pressure gradients). To put an additional constraint, we can compute the net torque induced by the Lorentz force, $\boldsymbol{T} = \int \boldsymbol{r} \times (\boldsymbol{J} \times \boldsymbol{B}) dV$, which is given as (Aly 1989)

$$T_x = -\frac{1}{8\pi}\int y(B_z^2 - B_x^2 - B_y^2) dxdy,$$
$$T_y = \frac{1}{8\pi}\int x(B_z^2 - B_x^2 - B_y^2) dxdy,$$
$$T_z = \frac{1}{4\pi}\int (yB_xB_z - xB_yB_z) dxdy, \quad (3)$$

where the origin of the coordinates (x, y) is set at the lower left corner of the magnetogram. Similarly, the normalized torques are defined as $t_x = |T_x|/T_p$, $t_y = |T_y|/T_p$, and $t_z = |T_z|/T_p$, and T_p is the magnitude of the net torque induced by only the magnetic pressure force, $T_p = |\int \boldsymbol{r} \times (\nabla \frac{B^2}{8\pi}) dV| = \sqrt{T_{px}^2 + T_{py}^2}$, where

$$T_{px} = \frac{1}{8\pi}\int y(B_x^2 + B_y^2 + B_z^2) dxdy,$$
$$T_{py} = \frac{1}{8\pi}\int x(B_x^2 + B_y^2 + B_z^2) dxdy. \quad (4)$$

A very important requirement in using the formula is that the magnetic field has a high-degree balance of the positive and negative fluxes, which can be quantified by the ratio of the net flux Φ_n to the total unsigned flux Φ_u,

$$e_{\rm flux} = \frac{\Phi_n}{\Phi_u} = \frac{\left|\int B_z dxdy\right|}{\int |B_z| dxdy}. \quad (5)$$

Last we note that since the formula of net force and torque, Equations (1) and (3), are integrations of the pixels of the magnetogram, they are not sensitive to the resolutions of the magnetogram (see also Jiang & Zhang 2019); for instance, we found that the results are almost unchanged by reducing the resolution of the original magnetogram with a factor of 2 or 4. Furthermore, we found that calculations of the force and torque are not very sensitive to the noise in the vector magnetograms. Bobra et al. (2014) state that, in the HMI vector magnetograms, the field strengths below 220 G are generally considered to be

noise. We have also calculated the forces and torques by using only the field above the noise threshold of 220 G, and found that they are changed very little, likely due to the fact that the contributions of the small-scaled, unresolved fields cancel each other in the integrations.

We survey all the space-weather HMI AR patches (SHARP; Bobra et al. 2014) with the definite NOAA number observed from 2010 May, when SDO began to operate, until the end of 2019. The following criteria are used to select the ARs. First, we focus on the emerging phase of ARs from almost nothing on the solar surface to its peak flux. Thus the ARs should have significant flux emergence during their passing on the solar disk, i.e., the total unsigned magnetic flux shows an evolution trend of overall monotone increase. Second, the target AR should be well separated from the surrounding ARs (presumably a single flux tube emergence and isolated from interaction with a significant preexisting field), so the positive and negative fluxes of the region can balance each other to a good degree, and in particular we only select the ARs with the flux-balance parameter $e_{\rm flux} < 0.1$ during their emergence phase. Third, to reduce the observation errors, we only select the duration when the ARs are located within $\pm 45^{\circ}$ in longitude from the Sun's central meridian (as will be shown in the next section, the distance of the observed AR to the solar disk center has a systematic influence on the magnitudes of the forces and torques). By all these criteria, we finally obtained 51 ARs with significant flux emergence during their passage on the solar disk. The ARs and their observed time durations are listed in Table 1, including their start and end times and their Carrington coordinates. The evolutions of total unsigned magnetic fluxes of all the ARs, calculated based on 1 hour cadence SHARP data and smoothed by a 6 hour window, are shown in Figure 1. As can be seen, overall the larger the AR's total flux is, the faster the AR emerges (Otsuji et al. 2011; Norton et al. 2017). With all the ARs considered, there are in total 3536 vector magnetograms obtained for our study to compute the forces and torques of the photospheric field.

We also take two typical, independently developed flux-emergence MHD simulations as a comparison with the observations. The two MHD simulations are obtained from Toriumi & Takasao (2017) and Syntelis et al. (2017), respectively, for the aim of reproducing the birth of ARs with significant nonpotentiality. Both simulations used typical settings of a twisted flux tube that is initially placed in the convection zone (with several megameters below the photosphere) and buoyantly rises to the photosphere, where it partially emerges into the corona. To compare the simulations with observations, it is crucial to use the same physical height of the photosphere. We note that in the simulations, the photosphere is slightly lifted by the emerging flux, and the buoyancy instability essentially happens at altitudes of approximately two scale heights (e.g., Fan 2009; Syntelis et al. 2017). Thus, we perform the force and torque computations using the magnetic field at three different heights, starting from z_0, which is closest to $z = 0$ in each numerical model, and moving upwards to the Parker instability height (z_2) at increments of around one pressure scale height.

3. Results

Before giving the statistical results, we first show the evolutions of two well-studied ARs, NOAA 11158 and 12673, and compare them with the two flux-emergence MHD simulations. Both the ARs have a fast flux-emergence phase during their passage on the solar disk and have strong nonpotentiality manifested by shearing and rotating motions of the emerging sunspots (Sun et al. 2012; Yang et al. 2017; Yan et al. 2018). As shown in Figure 2, both the ARs have significant flux increase, with an average emerging rate of $\sim 5 \times 10^{20}$ Mx h^{-1}, and their fluxes are very well balanced (with $e_{\rm flux} \sim 0.05$). The normalized forces and torques are mostly less than 0.1 for the full duration, suggesting that the field is very close to force-free in the emergence process. Note that for the normalized forces, our results are almost identical to those directly from the `cgem.Lorentz` data set.

In the simulations, although their flux contents are smaller by at least two orders of magnitude than the two ARs, their peak emerging rates are comparable to the observed ones. Since the two simulations use similar settings, they show very similar evolution, with a very fast rising and saturation of the fluxes in roughly an hour, while the observed ones have a steady flux increase for several days. The very distinct difference between the simulations and the observed ARs lies in the forces and torques: once the photospheric magnetic fluxes begin to increase in the simulations, the forces and torques in all three levels (see z_0, z_1, and z_2 labeled in the Figure 2) rise to significantly larger values ($\sim$0.8 for f_z) and torques ($\sim$0.6 for t_x and t_y), attaining the order of unity. This means that in the simulated cases, the balance between the tension and magnetic pressure gradient is strongly destroyed, i.e., in the extremely non-force-free state. For the z_0 level, this strongly forced state occurs during the entire emerging phase, while a little higher, the force and torque decrease systematically with time. In particular, in Syntelis et al.'s (2017) simulation, they decrease rather fast at z_2 where the Parker instability happens, reaching almost zero when the flux saturates. Therefore, our results show that during the flux injection phase, i.e., around the emergence rate peak, the forces and torques in typical flux emergence models are much larger than the observed ones. However, later, the dynamics settle to more realistic values. Note that it is due to the perfect symmetry of two emerging polarities in the simulations that the net forces in horizontal directions (i.e., f_x and f_y) and the net torques in vertical directions (t_z) are both zero.

Figure 3 shows the histograms of normalized forces and torques for all the 3536 magnetograms with both the average and median values denoted. The averages and standard deviations for the forces are, respectively, $f_x = 0.15 \pm 0.10$, $f_y = 0.13 \pm 0.08$, and $f_z = 0.13 \pm 0.08$. Thus all of them are close to 0.1, at which the field can be regarded as force-free (Metcalf et al. 1995). The median values of the forces are systematically smaller by a little bit than their average values. The averages and standard deviations for the normalized torques are, respectively, $t_x = 0.05 \pm 0.03$, $t_y = 0.11 \pm 0.07$, and $t_z = 0.12 \pm 0.09$. The torques show a slight dependence on the direction; t_x is approximately a half of t_y and t_z. In any case, on average, both the relative forces and torques of the magnetograms are close to 0.1, thus they can be regarded as being close to force-free. We note that with such a much larger set of emerging AR samples than previous statistical studies using the snapshots of developed ARs (Moon et al. 2002; Tiwari 2012), our results confirm that the photospheric field is actually not far from the force-free state, even in the dynamically emerging phase.

Table 1
NOAA Numbers, Durations, and Locations of All the Studied Flux Emerging ARs

No.	NOAA AR	Start Time	Longitude	Latitude	End Time	Longitude	Latitude
1	AR 11072	2010 May 21T08:00	−25.29	−13.63	2010 May 26T13:00	44.81	−14.24
2	AR 11076	2010 May 31T20:00	−6.78	−18.84	2010 Jun 4T16:00	44.47	−19.31
3	AR 11117	2010 Oct 26T04:00	4.30	18.27	2010 Oct 29T05:00	44.66	18.56
4	AR 11130	2010 Nov 28T08:00	−10.53	11.88	2010 Dec 2T10:00	44.58	12.39
5	AR 11141	2010 Dec 30T22:00	−3.05	37.20	2011 Jan 2T02:00	24.93	37.46
6	AR 11158	2011 Feb 12T14:00	−20.21	−14.39	2011 Feb 17T11:00	44.85	−14.17
7	AR 11327	2011 Oct 20T14:00	−18.73	−26.34	2011 Oct 24T01:00	27.38	−26.06
8	AR 11416	2012 Feb 8T14:00	−44.02	−11.58	2012 Feb 15T05:00	44.72	−11.22
9	AR 11422	2012 Feb 19T12:00	−9.89	22.59	2012 Feb 22T23:00	36.62	22.71
10	AR 11431	2012 Mar 4T12:00	16.26	−20.95	2012 Mar 6T16:00	44.67	−20.95
11	AR 11460	2012 Apr 18T01:00	−25.59	21.47	2012 Apr 23T00:00	41.11	21.04
12	AR 11551	2012 Aug 20T04:00	−11.20	5.26	2012 Aug 23T21:00	38.92	5.14
13	AR 11561	2012 Aug 30T01:00	−28.89	−19.08	2012 Aug 30T20:00	−18.18	−19.08
14	AR 11630	2012 Dec 8T12:00	−23.39	19.09	2012 Dec 11T10:00	15.65	19.47
15	AR 11640	2012 Dec 30T14:00	−23.17	30.84	2013 Jan 4T18:00	44.73	31.43
16	AR 11645	2013 Jan 2T20:00	−12.58	−10.24	2013 Jan 5T00:00	16.66	−9.98
17	AR 11682	2013 Feb 26T02:00	−9.25	−11.21	2013 Feb 29T00:00	29.82	−11.17
18	AR 11702	2013 Mar 20T19:00	10.00	15.09	2013 Mar 23T06:00	43.36	15.00
19	AR 11726	2013 Apr 19T06:00	−14.30	18.00	2013 Apr 23T14:00	44.80	17.60
20	AR 11750	2013 May 15T01:00	0.95	−7.33	2013 May 17T16:00	36.51	−7.63
21	AR 11764	2013 Jun 2T01:00	10.09	12.85	2013 Jun 4T00:00	36.56	12.61
22	AR 11765	2013 Jun 5T13:00	−24.40	10.51	2013 Jun 10T00:00	36.03	9.98
23	AR 11776	2013 Jun 20T05:00	12.50	9.24	2013 Jun 22T14:00	44.62	8.98
24	AR 11781	2013 Jun 27T21:00	−11.35	19.02	2013 Jul 1T00:00	30.25	18.66
25	AR 11784	2013 Jul 3T13:00	−11.31	−17.98	2013 Jul 5T00:00	8.33	−18.14
26	AR 11807	2013 Jul 28T11:00	−3.17	23.35	2013 Jul 30T12:00	23.58	23.20
27	AR 11813	2013 Aug 7T12:00	−0.32	−19.55	2013 Aug 10T00:00	33.42	−19.71
28	AR 11824	2013 Aug 17T11:00	4.51	−20.47	2013 Aug 19T17:00	34.87	−20.56
29	AR 11843	2013 Sep 17T08:00	−15.24	−6.14	2013 Sep 19T05:00	10.28	−6.12
30	AR 11855	2013 Sep 30T15:00	−20.03	−20.24	2013 Oct 4T00:00	25.52	−20.09
31	AR 11922	2013 Dec 10T01:00	5.96	9.86	2013 Dec 12T22:00	44.92	10.22
32	AR 11946	2014 Jan 5T16:00	−25.21	12.20	2014 Jan 10T00:00	33.55	12.69
33	AR 12003	2014 Mar 10T15:00	4.37	15.15	2014 Mar 13T13:00	44.00	15.12
34	AR 12089	2014 Jun 13T15:00	6.27	17.22	2014 Jun 16T12:00	44.81	16.87
35	AR 12119	2014 Jul 18T10:00	−23.26	−25.92	2014 Jul 23T00:00	37.78	−26.33
36	AR 12219	2014 Nov 25T13:00	−13.48	2.72	2014 Nov 29T20:00	44.89	3.24
37	AR 12234	2014 Dec 12T06:00	1.81	4.56	2014 Dec 15T00:00	39.22	4.90
38	AR 12257	2015 Jan 9T03:00	16.99	9.96	2015 Jan 10T20:00	40.20	10.13
39	AR 12273	2015 Jan 26T12:00	−8.98	2.86	2015 Jan 29T14:00	32.98	3.10
40	AR 12422	2015 Sep 24T19:00	−26.50	−26.83	2015 Sep 30T03:00	44.73	−26.63
41	AR 12530	2016 Apr 11T00:00	−2.54	21.03	2016 Apr 13T00:00	24.38	20.88
42	AR 12543	2016 May 9T06:00	−11.00	−2.04	2016 May 12T21:00	38.28	−2.42
43	AR 12571	2016 Aug 5T18:00	−12.30	7.86	2016 Aug 9T23:00	44.47	7.59
44	AR 12581	2016 Aug 29T22:00	19.07	5.11	2016 Aug 31T06:00	37.08	5.09
45	AR 12635	2017 Feb 8T17:00	−31.45	19.54	2017 Feb 13T09:00	31.55	19.79
46	AR 12673	2017 Sep 3T04:00	−8.37	−16.47	2017 Sep 6T06:00	33.44	−16.49
47	AR 12675	2017 Aug 30T23:00	8.50	−13.21	2017 Sep 1T11:00	28.88	−13.21
48	AR 12715	2018 Jun 19T11:00	−40.22	6.69	2018 Jun 20T22:00	−20.43	6.53
49	AR 12720	2018 Aug 23T21:00	10.78	0.83	2018 Aug 25T16:00	35.10	0.79
50	AR 12723	2018 Sep 29T15:00	−4.16	−16.11	2018 Oct 2T08:00	32.55	−15.98
51	AR 12733	2019 Jan 24T14:00	3.12	11.06	2019 Jan 26T21:00	34.26	11.26

Note. The longitude is Carrington longitude of the AR's center (i.e., the center of the SHARP patch) with respect to the disk center, in units of degree. The latitude is Carrington latitude of the AR's center, in units of degree.

To explore whether there are correlations between the forces (and torques) and key parameters during the flux emergence of ARs, such as the total unsigned magnetic flux Φ_u, the flux changing rate $d\Phi_u/dt$ and the nonpotentiality, which is quantified by the average twist parameter α_{tot} (Bobra et al. 2014) defined by

$$\alpha_{tot} = \frac{\int J_z B_z dxdy}{\int B_z^2 dxdy}. \quad (6)$$

The simple intuition is that, the faster the flux emerges, the larger the force should be; the more nonpotential or twisted the emerging field is, the larger the force and torque should be. In

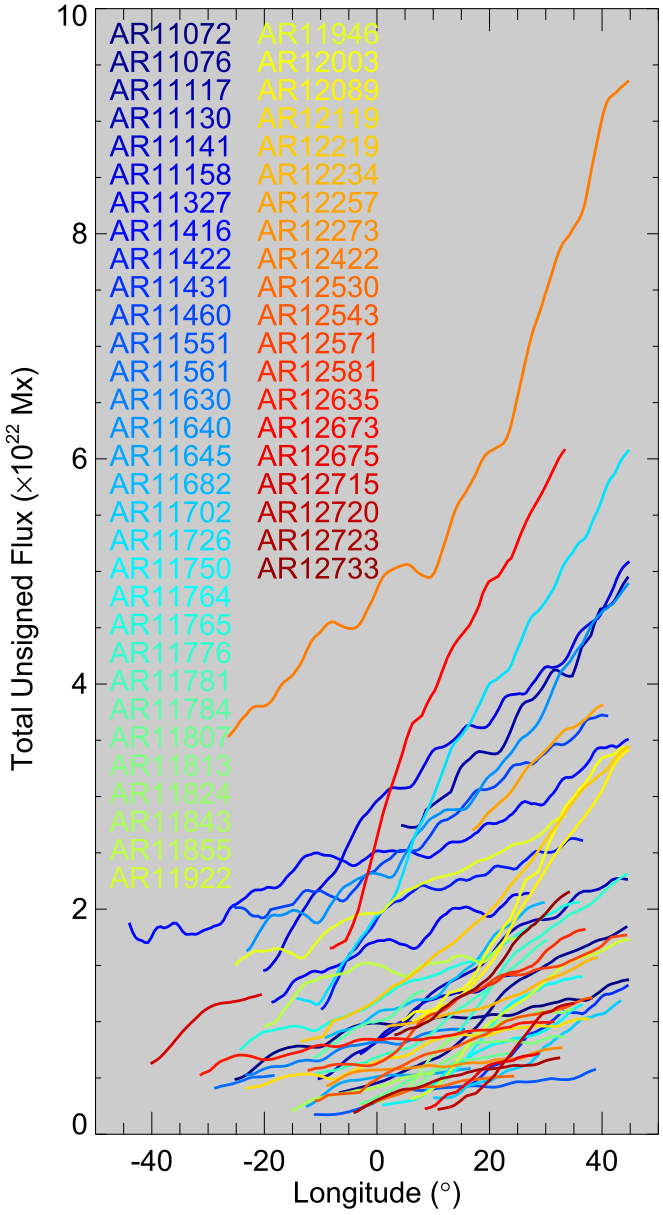

Figure 1. Magnetic flux evolution for all 51 flux emerging ARs. The horizontal axis shows the longitude of the AR's center with respect to the solar disk center, thus it also indicates the evolution time. Note that the events are selected with longitude between −45° and 45°. Different events are plotted in different colors, which denote the AR's number.

Figure 4, we plot the two-dimensional histogram showing the event frequency distributions in the two-parameter spaces defined by the force (and torque) with the three parameters Φ_u, $d\Phi_u/dt$, and α_{tot}, respectively. For simplicity, as we only care about the magnitudes, we use the average of the three components of force and torque by $e_{force} = (f_x + f_y + f_z)/3$ and $e_{torque} = (t_x + t_y + t_z)/3$. As can be seen, no systematic correlation is found between the forces (and torques) with either the total magnetic flux of the ARs, the emergence rates, or the nonpotentiality.

We further analyzed whether the force and torque are influenced by the observed locations of the ARs, since the further away from the solar disk center the target AR is, the larger the measurement errors would be. Indeed, as shown in the last column of Figure 4, an approximately linear correlation is seen in the force (and torque) with the distance of the observed AR from the disk center. It shows that the closer to the disk center, the smaller the force (and torque) is. Thus, the increase of the forces (and torques) is most likely due to the errors in the observations, and with a better quality of observed data, presumably the force and torque will be smaller, meaning that the emerging field is actually even closer to force-free than the results shown here.

4. Discussion

In this Letter, we have, for the first time, systematically surveyed the normalized magnitudes of the global Lorentz forces and torques in solar flux-emergence ARs observed by SDO/HMI. It is found that even during the flux-emergence phase, i.e., the formation of ARs, the magnetic field in the photosphere is generally close to the force-free state, since the relative measurements of the Lorentz force and torque are mostly on the order of 0.1. There seems to be no correlation between the magnitude of normalized force and torque with the total unsigned flux content of the emerging ARs, the emergence rate, or the nonpotentiality of the field. The only systematic correlation of the force (and torque) is found to be with the observed location of the ARs on the solar disk; that is, the closer to the solar disk center, the closer to force-free the field is. Therefore, this suggests that the actual magnetic field is even more force-free than what the statistic results show here. It can explain why many nonlinear force-free coronal-field extrapolations based directly on the photospheric vector magnetograms generally agrees with each other to some extent (e.g., Wiegelmann 2004; Valori et al. 2007; Wiegelmann & Sakurai 2012; Jiang & Feng 2013; Inoue et al. 2014), although there are still some mismatches between the models, and the mismatches can be further alleviated through a preprocessing of the vector magnetograms, in which the photospheric fields are able to be rendered highly force-free by adjusting the observed data within the noise level (Wiegelmann et al. 2006; Jiang & Feng 2014; Duan & Zhang 2018).

Our results show that during the emergence phase, idealized flux emergence simulations in which a twisted flux tube is artificially made buoyant to rise through the convection zone, show significantly larger forces (in comparison to the total magnetic pressure force) at the photosphere than the ones measured by our observations. It is after the flux injection phase, when the photospheric flux saturates, that the models tend to settle to more realistic photospheric force and torque ratios. This is suggestive of a discrepancy between simulations and observations. Very recently, using the flux emergence simulation of Toriumi & Takasao (2017) as a ground-truth data set (the same one we have analyzed in this Letter, as shown in Figure 2), Toriumi et al. (2020) performed a joint comparison of different data-driven coronal-field evolution models that use the photospheric magnetograms produced in the simulated flux emergence as input to their bottom boundaries (Cheung & DeRosa 2012; Jiang et al. 2016; Guo et al. 2019; Hayashi et al. 2019). It was found that, although all the data-driven models reproduced a flux rope structure, the quantitative discrepancies are large, which is attributed mainly to the highly non-force-free input photospheric field and to the treatment of background atmosphere. Especially, for a data-driven MHD model (Jiang et al. 2016) that used typical settings of the tenuous atmosphere in the corona (i.e., very low plasma β and high

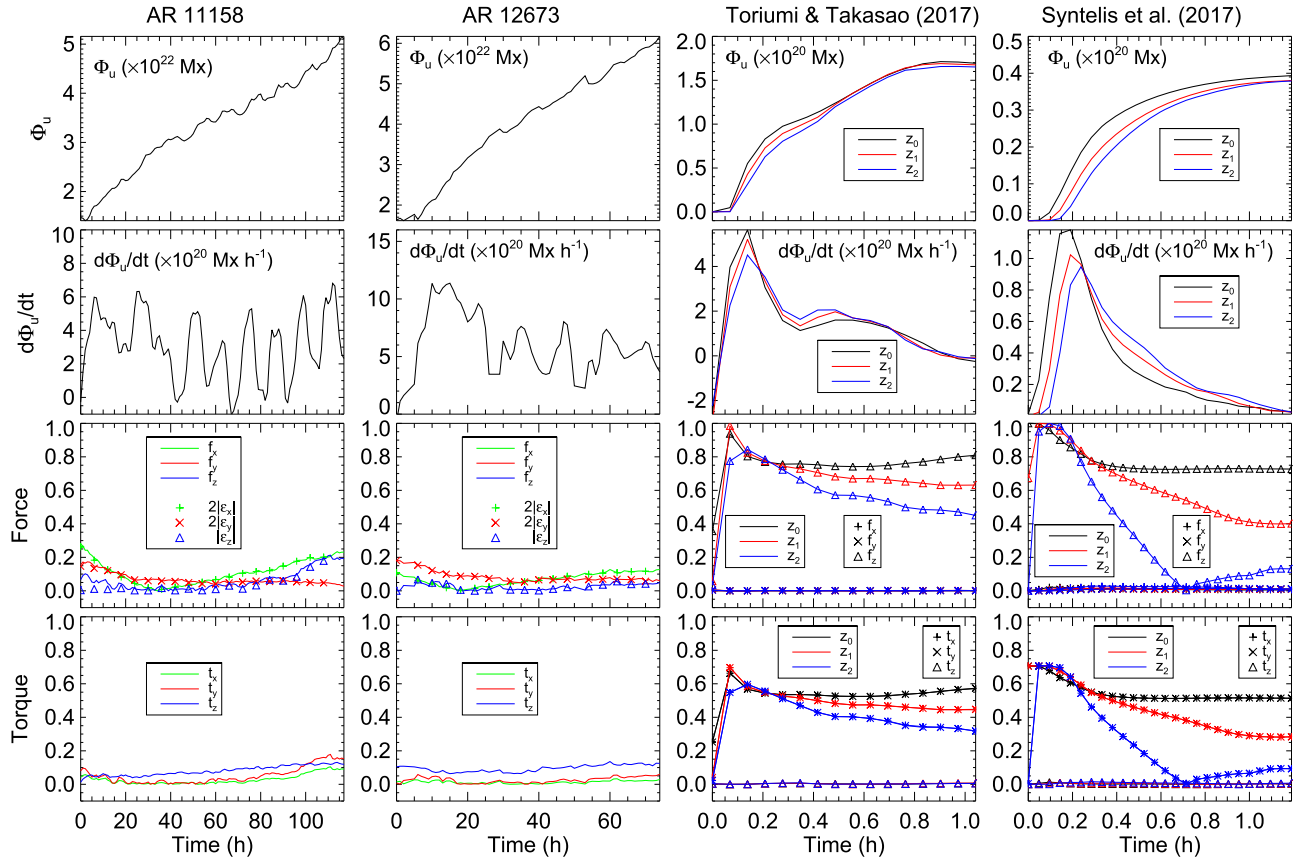

Figure 2. Comparison of different parameters from two observed flux-emerging ARs and numerical simulations. From top to bottom are, respectively, evolution of the total unsigned flux, flux emergence rate, normalized Lorentz force and torque. From left to right are results for AR 11158, AR 12673, simulations of Toriumi & Takasao (2017) and Syntelis et al. (2017), respectively. For the simulations we show the results for three different heights, which are $(z_0, z_1, z_2) = (0.14, 0.28, 0.42)$ Mm in Toriumi & Takasao's (2017) simulation, and $(z_0, z_1, z_2) = (0.12, 0.28, 0.43)$ Mm in Syntelis et al.'s (2017) simulation. The horizontal axes show the time for different events. Note that in the plots of normalized forces for the two ARs, the results from the `cgem.Lorentz` data set, i.e., ϵ_x, ϵ_y, and ϵ_z, defined in Sun (2014) are also shown for a double-checking of our calculations.

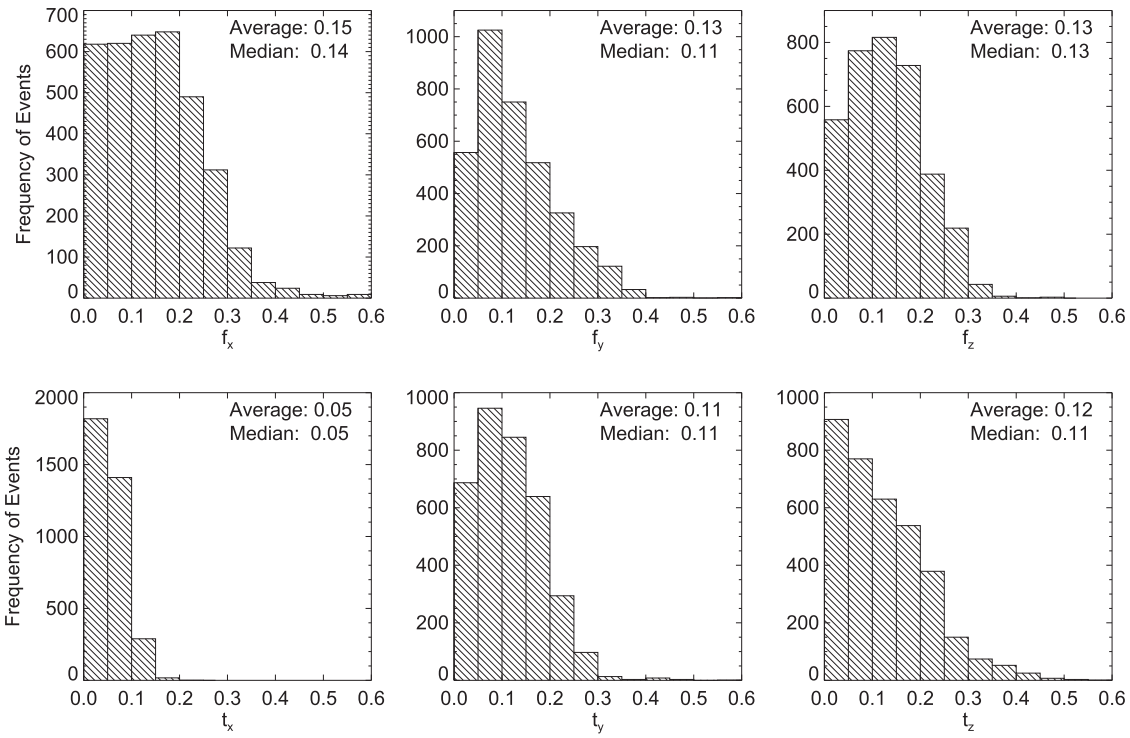

Figure 3. Histogram distributions of normalized Lorentz force f_x, f_y, and f_z (top panels) as well as torque t_x, t_y, and t_z (bottom panels) of a total number of 3536 magnetograms for all the analyzed ARs.

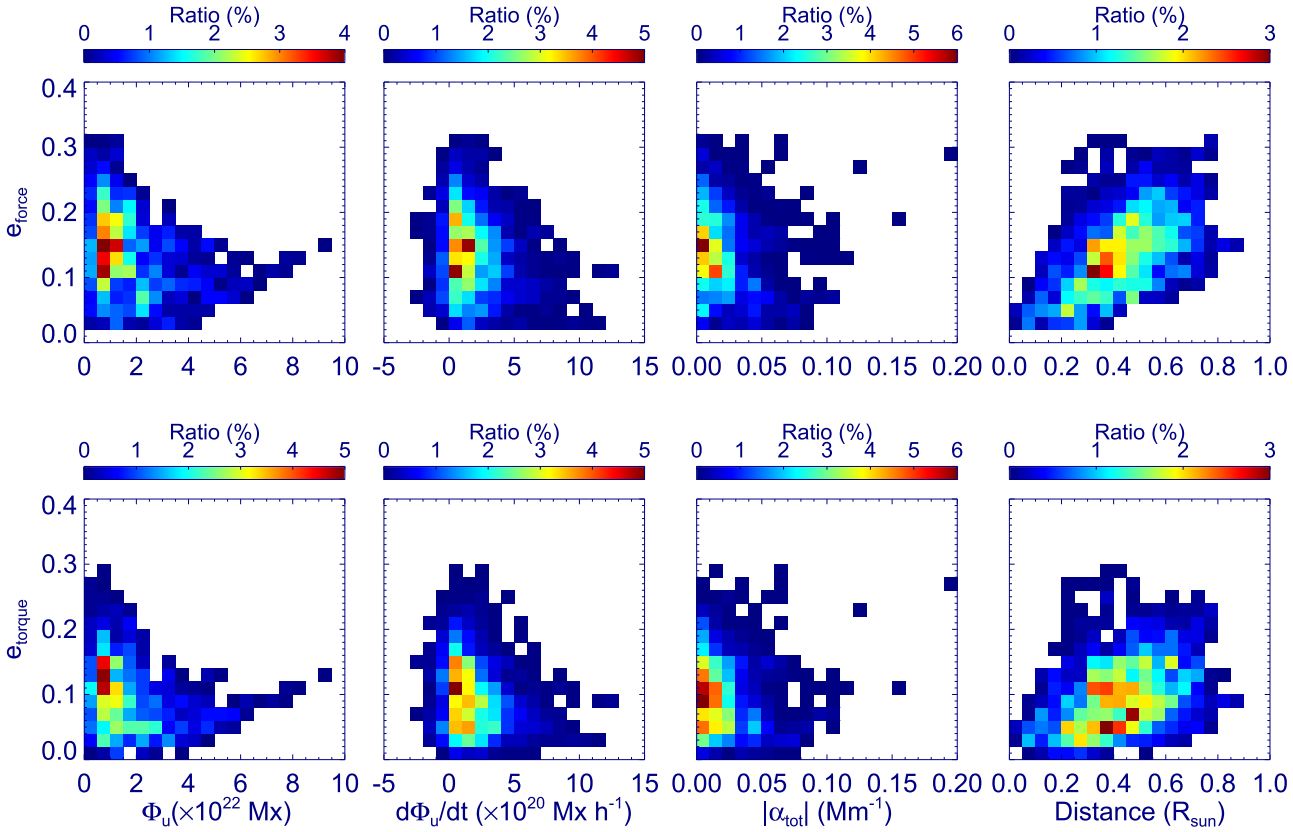

Figure 4. Distributions of magnetic force and magnetic torque with different parameters. The top panels are for magnetic force, and the bottom ones are for magnetic torque. The horizontal axes from the left to right columns represent, respectively, the total unsigned flux Φ_u, the flux changing rate $d\Phi_u/dt$, the mean twist parameter $\alpha_{\rm tot}$, and distance of the ARs from the solar disk center (in unit of solar radius $R_{\rm Sun}$). The colors indicate ratios of events in a specific bin. Here the bins for magnetic force and magnetic torque are both 0.02; and for Φ_u, $d\Phi_u/dt$, $\alpha_{\rm tot}$ and distance, they are 0.5×10^{22} Mx, 1×10^{20} Mx h^{-1}, 0.01 Mm^{-1}, and $0.02R_{\rm Sun}$, respectively.

Alfvén speed), the reproduced magnetic flux rope is significantly larger in size and stronger in field-line twisting than those in the original simulation as well as other data-driven MHD models that use typically dense plasma near the lower boundary (e.g., Guo et al. 2019; Hayashi et al. 2019). This discrepancy clearly arises from too strong Lorentz force of the simulated photospheric field, which cannot be balanced by the plasma in Jiang et al.'s (2016) model, and thus the flux rope can rise strongly upward and be freely twisted by the Lorentz force and torque, which leads to the strong magnetic energy and helicity in the corona. Thus, a further test of the data-driven models with more realistic and thus more force-free photospheric magnetic field needs to be done in the future.

By comparing the flux emergence rates from observations with those from typical MHD simulations, Norton et al. (2017) have found that the observed emergence rates are smaller than those in simulations, which indicates a slower rise of the flux in the interior than what is captured in simulations. That finding is consistent with ours, since with a slower emergence rate, the emerging field at the photosphere have more time to relax, and consequently be more force-free. In other words, the emergence at the photosphere might actually proceed in a quasi-static way rather than the dynamic one as shown in simulations. There are several aspects that can be adjusted in simulations to make the field emerge slower and thus, potentially, closer to force-free (and torque-free) in the photosphere. The first one is the depth where the initial flux tube is placed; both the simulations we used here have a flux tube placed near the solar surface, while with a flux tube placed much deeper in the interior, it can expand and stretch with more time to relax during its rising and should become more force-free than initially (e.g., Toriumi & Yokoyama 2011; Syntelis et al. 2019). The second one is the twist degree of the initial flux tube; stronger twist can of course create increased torque during its emerging in the photosphere (Sturrock et al. 2015; Sturrock & Hood 2016). The third one might be attributed to geometry of the emerging tube and how it couples with twist and the size of the flux tube, which has been discussed in Syntelis et al. (2019). Finally, including realistic turbulent convection in the modeling can further yield a much more relaxed emergence process (Toriumi & Hotta 2019). In summary, our study shows that the photosphere field is very close to force-free during the emergence process, and this fact should be taken into consideration in future development of MHD simulations as well as the theories of flux emergence.

This work is supported by the startup funding (74110-18841214) from Sun Yat-sen University. C.J. acknowledges support by the National Natural Science Foundation of China (41822404, 41731067, 41574170, and 41531073). S.T. was supported by JSPS KAKENHI grant Nos. JP15H05814 (PI: K. Ichimoto) and JP18H05234 (PI: Y. Katsukawa), and by the NINS program for cross-disciplinary study (grant Nos. 01321802 and 01311904) on Turbulence, Transport, and Heating Dynamics in Laboratory and Solar/Astrophysical Plasmas: "SoLaBo-X." P.S. acknowledges support by the ERC synergy grant "The Whole Sun." Data from observations are courtesy of NASA SDO/HMI science teams. We are

grateful to the anonymous referee for comments and suggestions that improved the paper.

ORCID iDs

Aiying Duan https://orcid.org/0000-0002-1916-1053
Chaowei Jiang https://orcid.org/0000-0002-7018-6862
Shin Toriumi https://orcid.org/0000-0002-1276-2403
Petros Syntelis https://orcid.org/0000-0002-6377-0243

References

Acheson, D. J. 1979, SoPh, 62, 23
Aly, J. J. 1984, ApJ, 283, 349
Aly, J. J. 1989, SoPh, 120, 19
Archontis, V. 2008, JGRA, 113, A03S04
Archontis, V., Moreno-Insertis, F., Galsgaard, K., Hood, A., & O'Shea, E. 2004, A&A, 426, 1047
Archontis, V., & Syntelis, P. 2019, RSPTA, 377, 20180387
Bobra, M. G., Sun, X., Hoeksema, J. T., et al. 2014, SoPh, 289, 3549
Cheung, M. C. M., & DeRosa, M. L. 2012, ApJ, 757, 147
Cheung, M. C. M., & Isobe, H. 2014, LRSP, 11, 3
Cho, I.-H., Cho, K.-S., Bong, S.-C., et al. 2017, ApJL, 837, L11
Duan, A.-Y., & Zhang, H. 2018, RAA, 18, 085
Fan, Y. 2009, ApJ, 697, 1529
Fisher, G. H., Bercik, D. J., Welsch, B. T., & Hudson, H. S. 2012, SoPh, 277, 59
Gary, G. A. 2001, SoPh, 203, 71
Guo, Y., Xia, C., Keppens, R., Ding, M. D., & Chen, P. F. 2019, ApJL, 870, L21
Hayashi, K., Feng, X., Xiong, M., & Jiang, C. 2019, ApJL, 871, L28
Hoeksema, J. T., Liu, Y., Hayashi, K., et al. 2014, SoPh, 289, 3483
Inoue, S., Hayashi, K., Magara, T., Choe, G. S., & Park, Y. D. 2014, ApJ, 788, 182
Jiang, C., & Feng, X. 2013, ApJ, 769, 144
Jiang, C., & Feng, X. 2014, SoPh, 289, 63
Jiang, C.-q., & Zhang, M. 2019, ChA&A, 43, 252
Jiang, C. W., Wu, S. T., Feng, X. S., & Hu, Q. 2016, NatCo, 7, 11522
Liu, S., & Hao, J. 2015, AdSpR, 55, 1563
Liu, S., Su, J. T., Zhang, H. Q., et al. 2013, PASA, 30, e005
Low, B. C. 1985, in Measurements of Solar Vector Magnetic Fields, Vol. 2374, ed. M. J. Hagyard (Washington, DC: NASA), 49
Metcalf, T. R., Jiao, L., McClymont, A. N., Canfield, R. C., & Uitenbroek, H. 1995, ApJ, 439, 474
Molodenskii, M. M. 1969, SvA, 12, 585
Moon, Y.-J., Choe, G. S., Yun, H. S., Park, Y. D., & Mickey, D. L. 2002, ApJ, 568, 422
Newcomb, W. A. 1961, PhFl, 4, 391
Norton, A. A., Jones, E. H., Linton, M. G., & Leake, J. E. 2017, ApJ, 842, 3
Otsuji, K., Kitai, R., Ichimoto, K., & Shibata, K. 2011, PASJ, 63, 1047
Parker, E. N. 1955, ApJ, 122, 293
Shibata, K., Tajima, T., Matsumoto, R., et al. 1989, ApJ, 338, 471
Sturrock, Z., & Hood, A. W. 2016, A&A, 593, A63
Sturrock, Z., Hood, A. W., Archontis, V., & McNeill, C. M. 2015, A&A, 582, A76
Sun, X. 2014, arXiv:1405.7353
Sun, X., Hoeksema, J. T., Liu, Y., et al. 2012, ApJ, 748, 77
Syntelis, P., Archontis, V., & Hood, A. 2019, ApJ, 874, 15
Syntelis, P., Archontis, V., & Tsinganos, K. 2017, ApJ, 850, 95
Tiwari, S. K. 2012, ApJ, 744, 65
Toriumi, S., & Hotta, H. 2019, ApJL, 886, L21
Toriumi, S., & Takasao, S. 2017, ApJ, 850, 39
Toriumi, S., Takasao, S., Cheung, M. C. M., et al. 2020, ApJ, 890, 103
Toriumi, S., & Yokoyama, T. 2010, ApJ, 714, 505
Toriumi, S., & Yokoyama, T. 2011, ApJ, 735, 126
Valori, G., Kliem, B., & Fuhrmann, M. 2007, SoPh, 245, 263
Wiegelmann, T. 2004, SoPh, 219, 87
Wiegelmann, T., Inhester, B., & Sakurai, T. 2006, SoPh, 233, 215
Wiegelmann, T., & Sakurai, T. 2012, LRSP, 9, 5
Yan, X. L., Wang, J. C., Pan, G. M., et al. 2018, ApJ, 856, 79
Yang, S., Zhang, J., Zhu, X., & Song, Q. 2017, ApJL, 849, L21